

Anion Exchange in Cationic Frameworks: Structures of Channel-Forming Triarylpyrylium Tetrafluoroborate Salts

Ren A. Wiscons,^{*,†} Matthias Zeller,^{‡,§} and Jesse L. C. Rowsell[†]

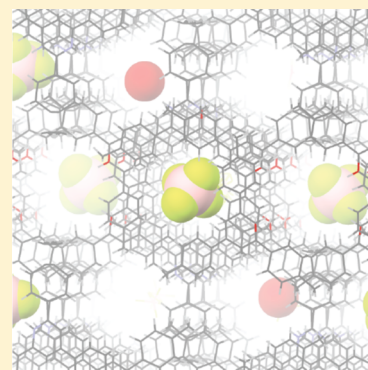
[†]Department of Chemistry and Biochemistry, Oberlin College, Oberlin, Ohio 44074, United States

[‡]Department of Chemistry, Youngstown State University, Youngstown, Ohio 44555, United States

[§]Department of Chemistry, Purdue University, West Lafayette, Indiana 47907-2084, United States

S Supporting Information

ABSTRACT: The crystal structure of a co-crystal of 2,4,6-tris(4-methylphenyl)pyridine and 2,4,6-tris(4-methylphenyl)pyrylium revealed a pseudo-hexagonal motif assembled from π -stacked helices that enclose 1-D channels containing disordered tetrafluoroborate counterions and solvent molecules. Though convoluted by disorder, aperiodicity, and complex twinning patterns, further investigation was motivated by the unique packing arrangement of this material, which enables solid-state anion diffusion, while resisting dissolution in water. Such properties are ideal for the development of anion exchange materials that can be employed for the remediation of agricultural and nuclear waste. To develop a more complete understanding of the intermolecular interactions that give rise to this helical motif, we have compiled and analyzed the local interactions and extended structural motifs of 19 pore- and channel-forming 2,4,6-triarylpyrylium crystal structures. Three conserved local interactions were identified, including C–H \cdots X[−] interactions, the rhombic binding pocket, and four-ring antiparallel dimerization. Development of this library of interaction motifs rationalizes the packing arrangement of the co-crystal and contributes to the informed design of anion exchange materials.



INTRODUCTION

Anionic species are central to many environmental and health-related crises such as eutrophication in wetland environments,^{1,2} unintended dispersal of vitrified radioactive waste,^{3,4} and introduction of organic acids and radioactive species (e.g., ^{99m}TcO₄[−] and ¹³¹I) into biogeochemical cycles.^{3–5} Though these concerns are pressing, selective noncovalent binding of anionic guests in cationic hosts is a relatively nascent focus of supramolecular chemistry. Challenges are, for example, presented by the size, solubility, and nondirectional electron density distribution of halides and spherical oxyanions (sulfates, phosphates, perchlorates, etc.).^{5,6}

The development of solid-state anion exchange materials remains a challenge, as the complexities intrinsic to heterogeneous-phase anion exchange are far from being well understood.^{1–9} One approach that has been investigated quite extensively is the use of molecular recognition for the selective entrapment of anions based on shape and electrostatic surface potential. Macrocyclic cages such as polyamide katapinands and cryptands encapsulate anionic guests in solution, thus preventing anions from interacting with other dissolved species.^{10–14} Most of these cages suffer from pH sensitivity and as a result are often not suitable for anion extraction from a broad range of aqueous environments. More recently, research groups have begun addressing these limitations by tuning weak C–H \cdots X[−] interactions for anion binding and by designing macrocycles that aggregate upon anion capture, allowing separation by filtration.^{14,16} Unfortunately, many of these

materials also have drastically lowered performances after moving from organic to aqueous exchange environments.^{6,9–16}

Increased attention has been dedicated to the design of metal–organic frameworks (MOFs) over the past decade with the goal of developing porous, robust, and tunable materials capable of selectively adsorbing gases for hydrogen storage, carbon-dioxide capture, liquid-phase separations, catalysis, and ion exchange.^{17–22} Anion exchange has long been recognized as a potential application of MOFs in which the organic ligands that define the distance between metal vertices are neutral, and anion entrapment arises as a result of balancing residual positive charge introduced by the metal coordination centers.⁵ Such materials allow for exchange under less extreme conditions than other materials may demand.²² MOF geometries are often restricted by directional bonding of linkers to the coordination geometries of metal centers.²³ Molecular crystals built from noncovalently interacting discrete molecular units are capable of accessing softer frameworks that can flex to accommodate guests of a nonideal size and defy the traditional geometric skeletons achievable by MOFs.²⁴

Pyrylium, a cationic heterocycle (Figure 1), introduces a unique opportunity to construct positively charged organic frameworks. As one of the most electronegative nuclei yet introduced into an aromatic system, the pyrylium's oxygen

Received: January 2, 2016

Revised: February 20, 2016

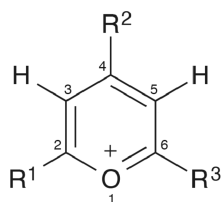


Figure 1. 2,4,6-Triarylpyrylium heterocyclic core.

atom induces a dipole moment on the heterocycle that polarizes the C–H bonds of carbon atoms C3 and C5 of 2,4,6-triarylpyrylium molecules,²⁵ which promotes its propensity toward anion binding in the solid state through reinforced C–H \cdots X[−] interactions.²⁶

Of the 21 known 2,4,6-triarylpyrylium-containing crystal structures (Cambridge Structural Database, CSD, surveyed in July 2015), 15 exhibit solid-state arrangements with continuous anion-containing channels or pores that are inherently compatible with reversible anion exchange and ion capture. In addition, three new crystal structures of solvated pyrylium salts and the crystal structure of a uniquely helical pyrylium/pyridine co-crystal are reported herein. These 19 triarylpyrylium-containing crystal structures (Figure 2) were analyzed to develop a library of intermolecular motifs persistent across pyrylium salts that display solid-state anion exchange potential. For each of the aforementioned 19 pore- and channel-forming triarylpyrylium crystal structures, we have modeled and compared the molecular conformations against the analogous triarylbenzenes and pyridines to understand the unique planarity and exocyclic bond deformation measured from the pyrylium cations.

The role of crystallization conditions and trapped solvent molecules in the local and extended motifs of solvated pyrylium frameworks was studied by characterizing the structural differences between the three new 2,4,6-tris(4-methylphenyl)-pyrylium tetrafluoroborate solvates crystallized from THF and water, acetic acid, and ethanol and water. These materials were found to decompose rapidly by hydrolysis in neutral and basic aqueous environments, limiting their functionality to acidic solutions. However, we have found that the solubility and stability of pyrylium salts in aqueous environments may be modified through co-crystallization with isosteric triarylpyridine molecules, extending the lifetime of this material in anion exchange settings and broadening the working pH range of pyrylium-based exchange material.

RESULTS AND DISCUSSION

Structural Organization in Triarylpyrylium Salts.

Coplanarity, though seen in triarylpyrylium molecules, is rarely observed in 1,3,5- and 2,4,6-triaryl-substituted arenes due to the barrier to planarization presented by steric clashing between hydrogen atoms on the central aromatic ring and hydrogen atoms on the substituent aryl rings. To investigate the origin of this coplanarity, mean values were calculated from torsion angles measured from populations of metal-free 1,3,5- and 2,4,6-triarylpyrylium, triarylpyridine, and triarylbenzene crystal structures obtained from the CSD (137 total structures) to determine whether the planarity observed from pyrylium compounds could be strictly attributed to a decreased barrier to rotation in heterocyclic systems. Alternatively, the low resonance energy of the pyrylium moiety may encourage near-planar molecular conformations, beyond what is observed in

triarylpyridine compounds, due to increased cross-conjugative demand.

Mean torsion angles between the central heterocycle and the aryl substituents *para* and *ortho* to the aromatic oxygen/nitrogen in triarylpyrylium cations (20.8° and 10.9°) and triarylpyridine (26.1° and 21.0°) molecules were measured and the average of all three torsion angles were calculated for triarylbenzene molecules (35.3°). The decrease in mean torsion angle between the triarylbenzene population and the triarylpyridine and pyrylium populations suggests that decreased hydrogen–hydrogen repulsion allows greater planarity, while significant differences in the mean torsion angles of the substituent arene *para* to the heteroatom calculated between the triarylpyridine and pyrylium populations suggests that triarylpyrylium cations gain thermodynamic stability by delocalization of positive charge across multiple rings by cross-conjugation.

The combination of hydrogen–hydrogen repulsion and coplanarity of the substituent rings with the core pyrylium heterocycle causes the mean exocyclic bond angles at position C2 and C6 on the triarylpyrylium ring, $\angle(\text{C}–\text{C}–\text{O}^+)$, to deviate from the idealized 120°, instead adopting angles between 112.2 and 116.8°. This deformation of exocyclic angles in triarylpyrylium salts was first observed in a 2,6-diphenyl-4-(4-nitrophenyl)pyrylium perchlorate salt (**8**) and was attributed to a combination of hydrogen–hydrogen repulsion and increased polarization of C–O⁺ bonds. The intermolecular bond distance between *ortho* hydrogen atoms on substituent aryls and the aromatic oxygen was found to be too long to be attractive, indicating that this deviation in angle is not attributed to intramolecular hydrogen bonding.³³

Computational models (B3LYP//6-31G(d))⁴⁰ of triarylpyrylium molecules **1** and **4–15** suggest that deviation from ideal σ C–C bond lengths between central and substituent rings, $d(\text{C}–\text{C})$, and exocyclic bond angles, $\angle(\text{C}–\text{C}–\text{O}^+)$, are positively correlated with the magnitude of the torsion angle between the central aromatic ring and the aryl substituents. Molecules **2** and **3** were excluded from analyses because coplanarity is enabled by the smaller size of the thionyl and methylfuranyl groups relative to the phenyl substituents. These calculations support the prediction that π -character of the bond connecting the central and substituent arenes (cross-conjugation) increases with decreasing torsion angle and drives, in combination with hydrogen–hydrogen repulsion, the deformation of exocyclic bond angles. In lieu of these findings, it is proposed that the tendency for triarylpyrylium cations to adopt torsion angles, $d(\text{C}–\text{C})$, and $\angle(\text{C}–\text{C}–\text{O}^+)$ that are lower than those measured for the identical triarylpyridine molecules is in part attributed to the electronic stability that can be gained by the pyrylium cation from substituent arene electron density donation.

Conserved Local Interactions in Solid-State Pyrylium Salts. Pore- and channel-forming triarylpyrylium salts adopt elaborate architectures that have a tendency to exhibit disorder, twinning, and stacking faults in the solid state, often leading to substantial non-Bragg behavior of their diffraction patterns and limiting the resolution of the crystal structures that can be obtained. The repeat sequence of the pyrylium framework and of the anions and solvent molecules in the channels are not necessarily commensurate with each other. More often than not, the content of the channels is ill defined, with problems ranging from simple disorder to completely diffuse electron density within the channels. Despite these substantial

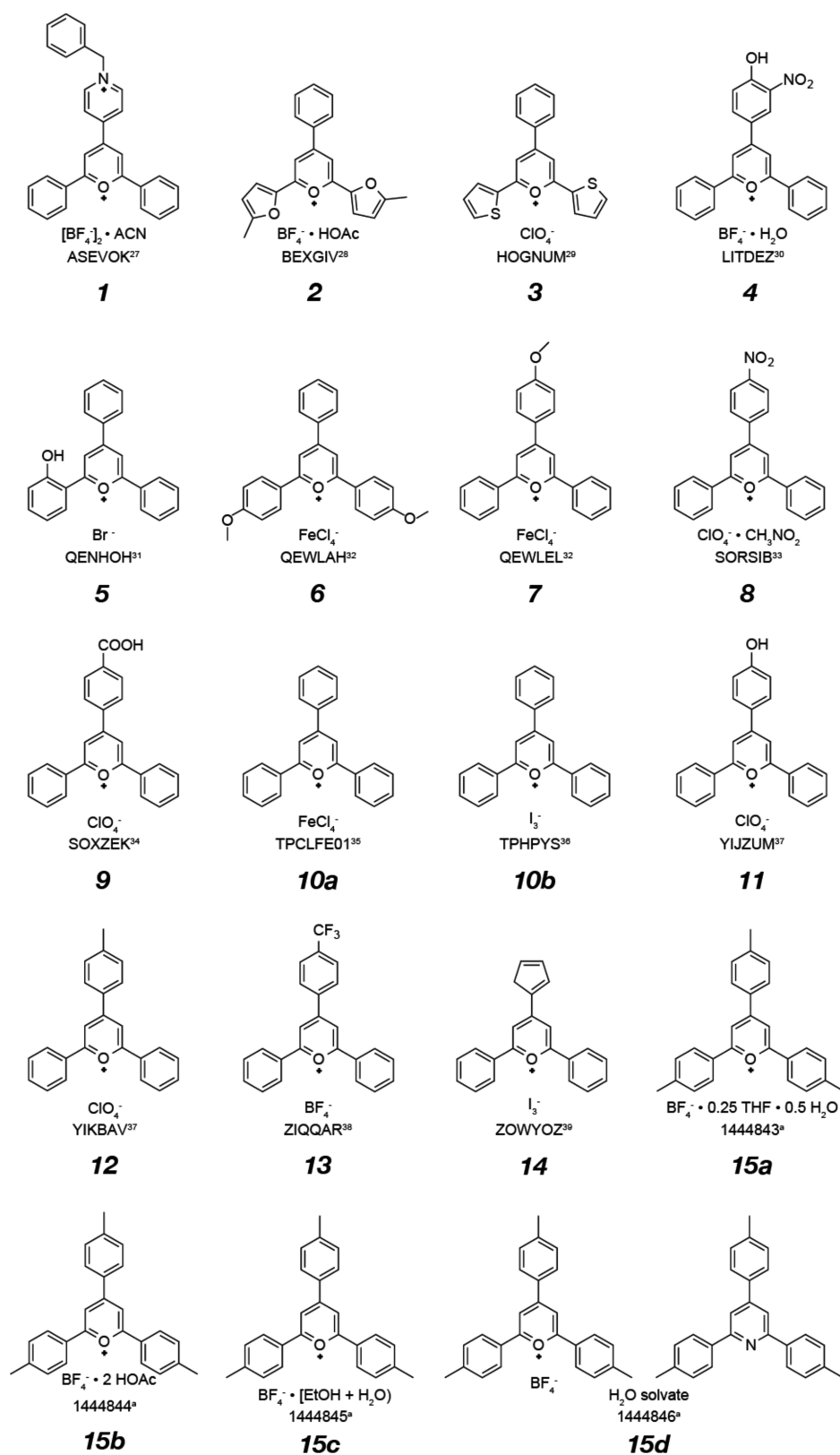


Figure 2. Crystal structures^{27–39} of pore- and channel-forming triarylpopyrylium salts sampled from the CSD (1–14) and reported in this article (15a–15d) that give rise to channelized solid-state materials. For structures 1–14, the codes given are the entry codes of the CSD, Cambridge Structural Database. ^aindicates the new triarylpopyrylium crystal structures reported herein.

challenges, enough data can be obtained from the available structures to elucidate some trends common to channel-forming triarylpopyrylium salts. The structures can be generally

understood as arising from a combination of three local geometries that persist across the 15 triarylpopyrylium crystal structures sampled from the CSD and four triarylpopyrylium

structures reported here for the first time. Of these crystal structures, 15 exhibit weak $C-H\cdots X^-$ interactions (Figure 3a),

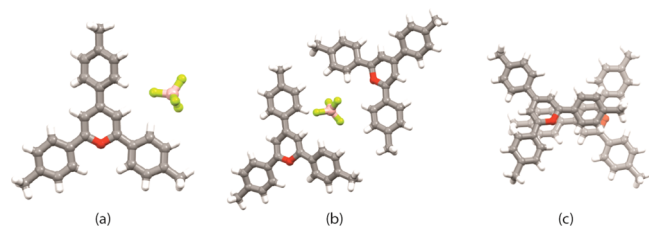


Figure 3. Conserved local motifs identified in triarylpyrylium salts including (a) reinforced $C-H\cdots X^-$ hydrogen bonding, (b) the rhombic anion binding pocket, and (c) four-ring antiparallel dimerization.

10 display two-molecule in-plane coordination of anions (Figure 3b), and 13 have four-ring antiparallel dimerization of triarylpyrylium molecules through cation- π aromatic stacking (Figure 3c).

Nonclassical $C-H$ hydrogen-bonds are not widely employed in crystal design due to their weakness relative to classical hydrogen-bond donor/acceptor pairs, though they often play an underlying role in crystal packing.^{15,41} However, in the case of pyrylium salts, the presence of the electronegative oxygen atom causes a substantial polarization of the triarylpyrylium core's $C-H$ bonds, which reinforces the strength of its $C-H\cdots X^-$ interactions²⁶ and makes these interactions a viable crystal engineering tool.

Previous groups studying the interactions between $C-H$ groups and O atoms have measured the hydrogen-bond-donating carbon to hydrogen-bond-accepting oxygen distances, $d(C\cdots O)$, as a proxy for $C-H\cdots O-C$ interactions, as the hydrogen atoms cannot be accurately located.⁴¹ Additionally, without experimentally determined hydrogen atom positions, the approach linearity between $C-H$ donors and acceptors can only be qualitatively described. For this reason, the $C\cdots X^-$ distances, $d(C\cdots X^-)$, between triarylpyrylium $C-H$ bond donors and anionic acceptors were measured for the 19 triarylpyrylium crystal structures that exhibit weak $C-H\cdots X^-$ interactions. Three $d(C\cdots X^-)$ were measured for each triarylpyrylium anion pair, a, b, and c (Figure 4).

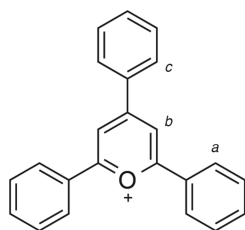


Figure 4. Carbon atoms for which the closest $C\cdots X^-$ and $C-H\cdots X^-$ distances were measured.

For more meaningful interpretation, the $H\cdots X^-$ contact distances were approximated by subtracting the idealized sp^2 $d(C-H)$ bond length, 1.2 Å,⁴² from the measured $d(C\cdots X^-)$ values. These hydrogen-normalized $d(C-H\cdots X^-)$ measurements were analyzed for $H\cdots X^-$ nonbonded radial overlap. It was found that all structures contained at least one $C-H\cdots X^-$ interaction in which the $d(C-H\cdots X^-)$ was shorter than the sum of the predicted nonbonded $H\cdots X^-$ contact distances,⁴² with

29% of the crystal structures containing only one short $d(C-H\cdots X^-)$, 29% of the structures containing two short $d(C-H\cdots X^-)$, and 41% containing all three short $d(C-H\cdots X^-)$. Structure-specific $d(C-H\cdots X^-)$ and radial overlap data are presented in the Supporting Information, SI.

The coplanarity of substituent aryl rings with the pyrylium core preorganizes a polydentate binding site for anions. When paired with that of a second triarylpyrylium molecule, this binding site mimics the geometry of macrocyclic anion receptors with a greater degree of flexibility with respect to the size of the target anion that can be accommodated. This motif is referred to as a “rhombic binding pocket” and persists in 63% of the pore- and channel-forming triarylpyrylium salt crystal structures. Triarylpyrylium salts that do not adopt this motif include those salts with notably large and/or soft anions (I_3^- , FeF_4^- , ClO_4^-) and pyrylium molecules with bulky aryl substituents, **1**. The predominance of the rhombic binding pocket in crystal structures suggests that this motif may exist as a precrystallization complex and potentially in solution as a homogeneous-phase anion receptor in addition to solid-state triarylpyrylium exchange materials (Figure 5).

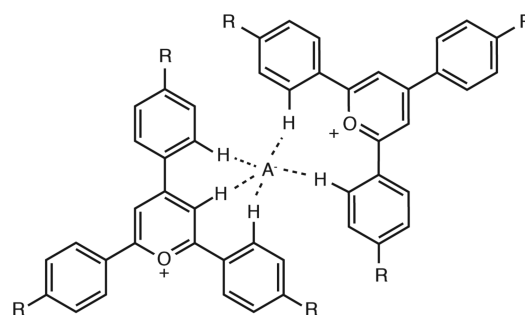


Figure 5. Mimicry of macrocyclic anion binding by the rhombic binding pocket.

The final conserved local geometry does not involve interactions with anions but is limited to the pyrylium framework. This interaction arises as a result of cation- π -facilitated face-to-face aromatic stacking (Figure 6) in which a substituent aryl ring (A) participates in aromatic stacking interactions with the pyrylium heterocycle (B) on the molecule above/below and vice versa, heterocycle (C) to substituent (D). Lateral slipping lengthens the centroid-centroid distance between rings (A) and (B) and (C) and (D) with the longest centroid-centroid distance measured at 4.158 Å and the shortest at 3.436 Å. The four-ring antiparallel dimerization geometry is adopted by all pore- and channel-forming triarylpyrylium salts with the exception of the triiodide salts (17 structures), in which π -stacking is disrupted by aromatic sandwiching of the triiodide anion.

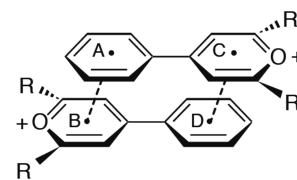


Figure 6. Centroid-to-centroid (A \cdots B and C \cdots D) distance measurements for the four-ring antiparallel dimerization.

Role of Crystallization Solvent in Pirylium Architectures. Solvent choice is often critical in accessing specific polymorphs in systems that express geometrical frustration and in crystallizing soft supramolecular assemblies. Though the individual interactions between solvent molecules and precrystalline complexes are only loosely understood, trapped solvent molecules and the inherent disorder in positions, orientations, and conformations of these molecules in triarylpyrylium solvates play a fundamental role in the control of channel morphology in the solid state. Of the 19 triarylpyrylium salts, 8 structures are solvates, 7 of which contain solvent molecules that are crystallographically well enough defined to be modeled and refined.

Solvents capable of accepting C–H...X[−] hydrogen-bonds, such as acetic acid, ethanol, nitromethane, and water, were found noncovalently bound to the framework by accepting hydrogen-bonds donated by C3–H and/or C5–H of the pyrylium heterocycles. THF, a solvent molecule less inclined to form hydrogen-bonds with the framework, is instead surrounded by the triarylpyrylium substituents donated by six separate molecules and is more severely disordered in the crystal structure, indicating that the interaction between the solvent molecule and framework is nonspecific compared to the hydrogen-bond-accepting solvents. These solvent coordination motifs give rise to the two general solvent pocket structures that, when alternated with the rhombic anion binding pocket, result in the diversity of channel types observed in triarylpyrylium materials (Figure 7).

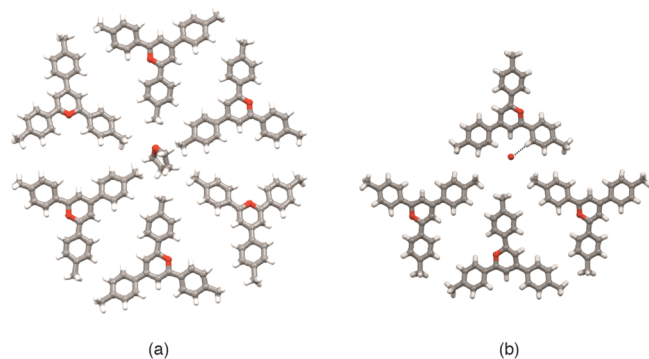


Figure 7. Conserved local solvent pockets, including the nonpolar (a) THF pocket and (b) the hydrogen-bond acceptor pocket with a water molecule located within the weak hydrogen-bonding distance (2.787 Å) from the polarized pyrylium C–H, which is indicated by a dashed line.

Persistent Extended Motifs in Solid-State Pirylium Salts. Poor diffraction quality arising from disorder, twinning, and stacking faults suggests that the combinations of local interactions that give rise to extended triarylpyrylium motifs are nonspecific relative to conventional crystal engineering syntheses. Channels of variable morphologies arise from the alignment and alternation of the two-dimensional solvent and rhombic anion binding pockets. Trapped solvent stabilizes the channel continuity by screening anion–anion Coulombic repulsion. Additionally, the character of the solvent can determine the patterning of the inner channel walls with the electrostatic character of the triarylpyrylium molecule's substituent by promoting alternation of a particular solvent pocket type to form the channel.

To directly study the effect of solvent type on triarylpyrylium salt frameworks, we built a library of three such patterns within a series of 2,4,6-tris(4-methylphenyl)pyrylium tetrafluoroborate (TMPPyry⁺ BF₄[−]) solvated salts. TMPPyry⁺ BF₄[−] was synthesized by an acid-catalyzed cyclocondensation adapted from the literature⁴³ (synthetic details available in the [Experimental Section](#)). In all three solvates, the nonpolar character of the TMPPyry⁺ methyl substituents gives rise to various hydrophobic barriers to anion mobility diagrammed in [Figure 8a–c](#). These nonpolar barriers have been labeled

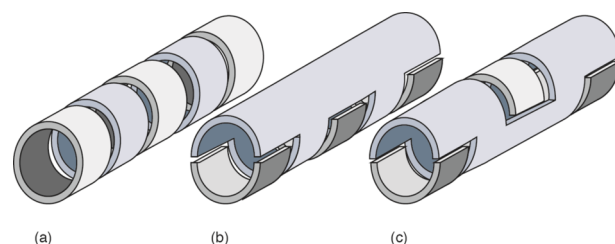


Figure 8. Diagram of inner channel wall nonpolar barriers to anion diffusion with polar surfaces shown in blue and nonpolar surfaces in gray: (a) elliptical, (b) parabolic, and (c) alternating parabolic.

elliptical, parabolic, and alternating parabolic. A detailed understanding of these patterns enables precise control over the steric and electrostatic barriers encountered by mobile anions during exchange and can be exploited in order to design and tune anion exchange materials that are selective for particular guests. These electrostatic surfaces, in addition to steric barriers, affect the mode of anion binding. The following two sections discuss, in detail, how channel structures may be combined to synthesize anion exchange materials within a series of TMPPyry⁺ BF₄[−] solvated salts and co-crystals.

Solvates of 2,4,6-Tris(4-methylphenyl)pyrylium BF₄[−] Salts. The one-pot synthesis of TMPPyry⁺ takes place by reacting two molar equivalents of 4-methylacetophenone with one molar equivalent of 4-methylbenzaldehyde in the presence of boron trifluoride to form the central pyrylium cation.⁴³ The TMPPyry⁺ BF₄[−] solid was then recrystallized solvothermally from various solvents.

A THF and water solvate of TMPPyry⁺ BF₄[−] (**15a**) can be crystallized from a biphasic THF/water solvent mixture. The solvent molecules are located in channels and alternate with tetrafluoroborate anions ([Figure 9a](#)). The two types of solvent molecules give rise to two different channel morphologies as a result of the variable hydrogen-bond-forming capabilities of the two molecules. The first channel type arises from alternation of tetrafluoroborate anions and THF molecules. The THF molecules, incapable of forming strong hydrogen-bonds (relative to protic solvent molecules), are surrounded by methyl substituents from six separate TMPPyry⁺ molecules, giving rise to elliptical nonpolar barriers to anion diffusion ([Figure 8a](#)). Because interactions between the THF molecules and the framework are nonspecific, THF molecules are 2-fold rotationally disordered in the solid state. The second channel type contains tetrafluoroborate anions and water molecules and exhibits a parabolic nonpolar electrostatic patterning of the channel surface ([Figure 8b](#)). This patterning arises as a result of the water molecules' hydrogen-bonds to the framework bringing three methyl groups to one side of the channel and acidic C–H moieties on the other. Individual water molecules are engaged in four hydrogen-bonds, accepting two C–H

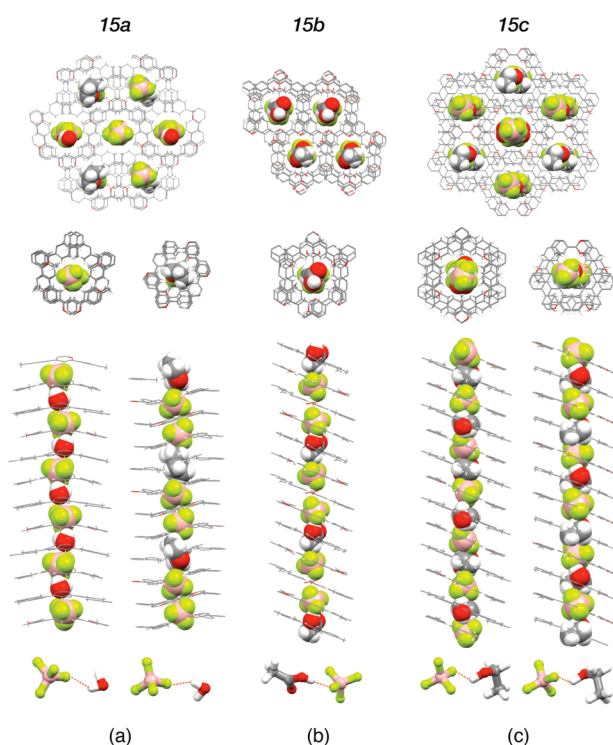


Figure 9. Channel structures of (a) **15a**, (b) **15b**, and (c) **15c**, highlighting the channel cross-section, the solvent molecule and tetrafluoroborate repeat sequence in the channel, and the hydrogen-bonding interaction in each of the crystal structures between the solvent and tetrafluoroborate.

groups from the framework (from two *ortho* phenylene groups) and donating two O–H...F hydrogen-bonds to the tetrafluoroborate anions in the channel, forming a chain of hydrogen-bonded guest molecules (Figure 9a).

The acetic acid solvate of the TMPPy⁺ BF₄[−] salt (**15b**) forms a complicated series of channels containing the tetrafluoroborate anions and two types of disordered acetic acid dimers that exhibit the typical R₂²(8) carboxylic acid dimer H-bonding motif. Continuous aromatic stacking between the cations is disrupted by π – π interactions between acetic acid dimers and the tolyl substituent of a neighboring TMPPy⁺ cation with a centroid-centroid stacking distance of 3.411 Å. Intercalation of the acetic acid dimers between TMPPy⁺ molecules limits aromatic stacking interactions to discrete cation- π -facilitated stacked TMPPy⁺ dimers. The acetic acid dimers are the sole occupants of continuous channels parallel to the *c*-axis. A second set of channels propagates parallel to the *a*-axis and contains alternating tetrafluoroborate anions and acetic acid molecules (Figure 9b) with an alternating parabolic nonpolar channel surface pattern (Figure 8c). The acetic acid molecules in the second channel type accept hydrogen-bonds donated by the framework and donate C–H...O hydrogen-bonds to the tetrafluoroborate anions within the channel, forming a directional solvent-anion hydrogen-bonded chain (Figure 9b).

Solvothermal crystallization of the TMPPy⁺ BF₄[−] salt from an ethanol and water mixed solvent system yields crystals with two channel types containing chains of tetrafluoroborate anions and solvent molecules: alternating and continuous parabolic channel surface patterning (**15c**). Both channel types contain ethanol molecules, though one of the channel types is found to

contain water molecules as well, consistent with the dependence of this phase crystallizing out of a solvent solution doped with water (see SI for more details). The two channel types are differentiated by the orientation, disorder, and interactions of the ethanol and water molecules relative to the surrounding framework. In both channels, ethanol molecules and tetrafluoroborate anions are connected via strong O–H...F hydrogen-bonds, forming solvate–anion pairs (Figure 9c). Channels containing ordered ethanol molecules are nearly trigonal cross-sectionally, accepting hydrogen-bonds donated by framework molecules that bond to the well-ordered solvate-anion pairs within the channel. The contents of the second channel type refined to an 86% ethanol and 14% water occupancy. The disordered solvent molecules are arranged around a crystallographic 2-fold axis, imposing additional whole ethanol molecule disorder. The symmetry imposed solvent molecule disorder breaks the directionality of the O–H...F hydrogen-bonds leading to anion disorder as well. This disorder is likely correlated with the larger channel diameters of the second channel type, offering greater conformational flexibility of the ethanol molecules and greater mobility of the tetrafluoroborate anions.

Co-crystals of 2,4,6-Tris(4-methylphenyl)pyrylium BF₄[−] and 2,4,6-Tris(4-methylphenyl)pyridine. Co-crystallization has been identified as a nonsynthetic means by which to attenuate physical properties of solids, such as the bioavailability of pharmaceuticals, the sensitivity and detonation velocity of energetic materials, and the solubilities of solids. Co-crystals of TMPPy⁺ BF₄[−] and 2,4,6-tris(4-methylphenyl)pyridine, TMPPy, (**15d**) crystallized from a biphasic THF and water solvent mixture, exhibit both a new extended structural phase not observed in pure-phase triarylpyrylium salts and decreased solubility in water, a property desirable for anion exchange materials to be utilized in natural settings.

Co-crystallization of TMPPy⁺ BF₄[−] and TMPPy was attempted as a method by which to stabilize TMPPy⁺ BF₄[−] solids in water. As a result of the oxygen atom's electronegativity, pyrylium reactivity differs greatly from that of benzene and pyridine, having weaker resonance energy and a greater susceptibility toward nucleophilic attack. This phenomenon makes the pyrylium cation subject to rapid decomposition when dissolved in water. Though this hydrolysis can be slowed and even reversed in acidic solutions, co-crystallization with isosteric pyridine compounds was predicted to slow dissolution, protecting against pyrylium hydrolysis in aqueous environments of unknown pH.

The pyridine derivative, TMPPy, was prepared by reacting two molar equivalents of 4-methylacetophenone with one molar equivalent of 4-methylbenzaldehyde in the presence of an acid catalyst, acetic acid, and a large excess of ammonium acetate to form the central pyridine ring.⁴⁴ TMPPy⁺ BF₄[−] and TMPPy can be co-crystallized from a 1:1 molar ratio of the two solids in a 1 THF: 1 water (v/v) solvent mixture. The compounds are dissolved by heating the suspension in THF/water to 70 °C, inducing phase separation of the system. Slow cooling of the system to 4 °C causes collapse of the separated phases, and bright red crystals are obtained (details provided in the Experimental Section).

The co-crystal structure has been solved and refined in the orthorhombic space group *Fddd*, but is convoluted by disordered anions and solvent molecules in the channels, solid solution disorder of the pyrylium cations and pyridine molecules, and twinning through pseudomerohedry emulating

a hexagonal primitive packing; initial structure solutions modeled in $P2_1$, a subgroup of the actual space group $Fddd$ not obscuring the pseudo-hexagonal lattice dimensions, refined with a β -angle of 119.759° and a - and c -axes of 38.5754 and 38.6371 Å, respectively and refined to a 2.125 TMPPyry⁺ BF₄⁻: 0.875 TMPPy molar ratio. Though solid solution of the TMPPyry⁺ BF₄⁻ and TMPPy prevents these molecules from being definitively discerned from one another in the crystal structure, a UV–vis absorbance shift of the co-crystalline solid relative to pure-phase triarylpyrylium solids suggests a strong electronic interaction between the pyridine and pyrylium moieties. Such an interaction is predicted to provide electron density to the core pyrylium cation, stabilizing the heterocycle.

The solid solution between TMPPyry⁺ BF₄⁻ and TMPPy molecules in this system was explored by ¹H NMR and powder XRD, PXRD, (Figure 10a, b). Precrystallization molar ratios

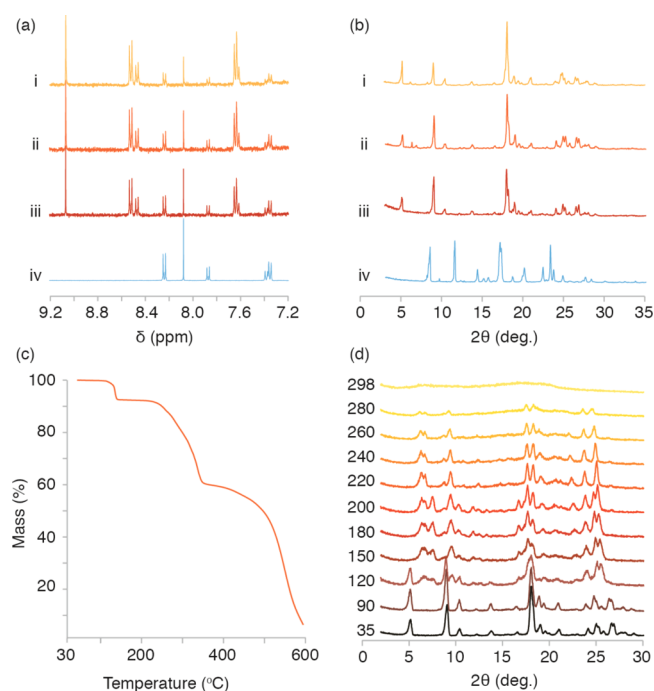


Figure 10. Solid solution, thermal, and structural properties of **15d**. (a) ¹H NMR spectra and (b) PXRD of bulk co-crystalline material of variable mole percent TMPPyry⁺: 81% (i), 71% (ii), 68% (iii), and 0% (iv) crystallized from starting mass ratios of 90%, 70%, 50%, and 10% TMPPyry⁺ BF₄⁻. (c) TGA and (d) VT-PXRD of co-crystal bulk revealing structural deformation and retained crystallinity upon solvent evacuation with the temperature (°C) at which each pattern was taken indicated to the left of the pattern.

between the two species were varied in 10% intervals and the final stoichiometries of the resultant co-crystals determined by integration ratios of ¹H NMR peaks of redissolved crystals. It was found that the co-crystals have to contain between 68 and 81 molar percent TMPPyry⁺ in order to form the co-crystalline structural phase. Above and below of this range, crystals of pure TMPPyry⁺ BF₄⁻ and colorless crystals of TMPPy are formed beside the bright red solid solution co-crystals. Solid solution of the framework molecules contributes to guest disorder, as a variable number of counteranions must be entrained in the channels in order to charge balance the framework. Minimal peak shifts in the PXRD patterns (Figure 10b) support a conserved co-crystalline structural phase across solid solution

compositions, while a variation in lattice site occupancy can be predicted from changes in relative peak intensity.

Variable temperature PXRD, VT-PXRD, and thermogravimetric analysis, TGA, (Figure 10c, d) reveal that mobilization of trapped solvent is correlated with anisotropic distortion of the helical channels. This can be observed by PXRD peak-splitting and symmetry changes that result from heating bulk samples of the co-crystal. The quality of the single crystals was severely compromised, preventing more detailed structural analysis of the desolvated co-crystalline phase. These results suggest flexibility of the framework to accommodate guest diffusion and exchange.

The 2-fold triple helical channels arise from a series of twisted and interlocked rhombic binding pockets (Figure 11b),

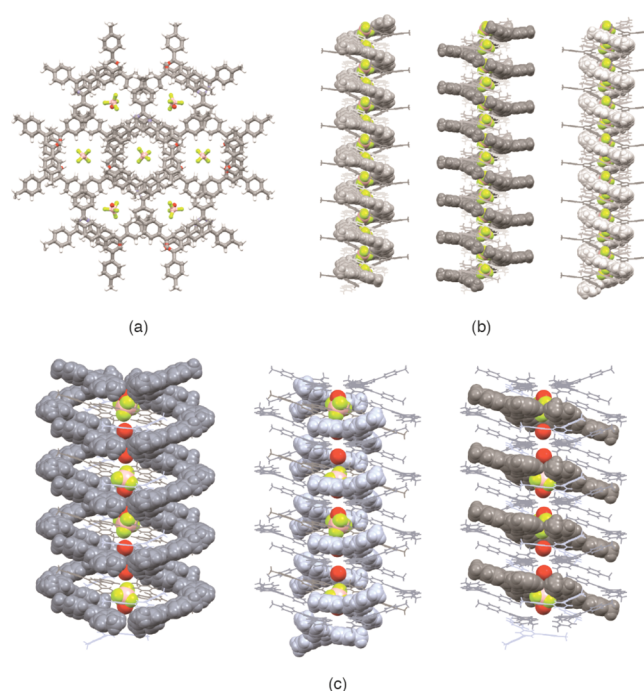


Figure 11. Crystal structure of **15d** in $Fddd$ (a) parallel to the a -axis, illustrating the two major channel types: (b) the 2-fold triple-helical pseudo-hexagonal channel of rhombic binding pocket motifs and (c) the alternating parabolic channel.

and as a direct result, the inner channel environment lacks nonpolar patterning from the methyl substituents. Difference density $F_o - F_c$ maps of the single crystal data confirm that both channel types enclose disordered anions and solvent molecules. Atomic positions are not well resolved, though the helical channel contains guests that are better defined than the completely diffuse electron density enclosed by the second channel type. The framework of the second channel type (Figure 11c) is built from the alternation of the polar solvent pocket, Figure 7b, and rhombic binding pockets, resulting in an alternating parabolic channel surface, which provides diffusing anions with a continuous helical path. The difference in resolution of the channel guests is most likely attributable to a difference in mean solvent occupancy between the two channel types, one channel containing predominantly anions, which can form more favorable interactions with the walls of the triple-helical channel and the other containing disordered water molecules.

Two structural roles can be assigned to TMPPy that cause the motifs unique to the co-crystal structure to deviate from those adopted by the pure-phase pyrylium salts and solvates: as an isosteric uncharged structural spacer and as a solubility modifier.

The triple-helical channel observed in the co-crystal is the only extended motif observed in the TMPPy⁺ BF₄⁻ series that does not exhibit alternation between solvent and anionic binding pocket types, but it instead exclusively contains twisted interlocked anion binding geometries. The tetrafluoroborate anion has a van der Waals radius of approximately 4.32 Å, though the space available for a counteranion in an individual rhombic pocket in the triple helix is only 3.62 Å, due to interlocking of the rhombic anionic binding pockets. The helical morphology cannot arise in pure TMPPy⁺ BF₄⁻ crystal structures because there is not enough space available to accommodate the number of BF₄⁻ anions required to charge-balance the framework. The helical morphology is allowed in the co-crystal because the TMPPy molecule serves as a spacer to alleviate charge balance complications that arise from the uninterrupted stacking of anions in the binding pockets. ¹H NMR spectra of redissolved co-crystals show a solid solution between the two heterocyclic molecules, suggesting that this intercalation is necessary to relieve frustration, but diffraction reveals that this replacement does not occur in predictable lattice positions in the crystal structure.

The second major role of the TMPPy is its notable modification of TMPPy⁺ BF₄⁻ salt solubility in aqueous media, which is an important feature in developing anion exchange materials that are useful and efficient in natural aquatic settings. The strong electronic attraction between the pyrylium and pyridine moieties greatly extends the lifetime of the material in water by decreasing the solubility of the material thus preventing hydrolysis of dissolved triarylpyrylium cations.

The Mechanisms of Anion Exchange. Theory and mechanistic details of anion separation as they apply to potential exchange in triarylpyrylium cationic frameworks and other solid-state materials have been presented elsewhere^{5,44} but will be briefly summarized here. The three predominant mechanisms include heterogeneous-phase anion diffusion,⁵ homogeneous-phase competitive crystallization,⁵ and synthetic anion exchange.⁴⁴ Ideal heterogeneous anion exchange materials facilitate anion diffusion through the salt lattice at a rate much faster than that of framework dissolution,⁵ thus leaving the framework functionally intact. Viability of heterogeneous exchange can be limited by structural deviation between the frameworks of the original and exchanged salts and can be biased for anions less soluble in the exchange media due to variable enthalpy changes during anion desolvation as the dissolved and framework anions swap.⁵ Solvation bias, though still present, may be lessened in homogeneous-phase exchange settings by receptor complementarity. Anion separation by selective crystallization is here defined as partial or complete dissolution of the crystal followed by reprecipitation of a salt encasing the target anionic guest. This separation mechanism is driven by a significant difference in solubility between the initial and exchanged salts⁵ and, unlike heterogeneous exchange, the lattice isorectricity need not be retained. The third exchange method, synthetic anion exchange, is not subject to solvation bias and proceeds by taking advantage of the pH-reversible charged and uncharged states of substituted pyrylium compounds. Synthetic anion exchange is a brute-force method of exchange by hydrolysis of the pyrylium ring to a substituted

neutral pentenedione/pentadieneone and recyclization with the acid or aqueous inorganic salt of choice to reform the pyrylium cation.^{4,44–46} Preliminary results suggest that *15d* is capable of undergoing anion exchange through either heterogeneous and homogeneous exchange mechanisms depending on the nature of the anion, as supported by PXRD and IR studies (see SI for more details).⁴⁶

CONCLUSIONS

With great structural diversity in extended cationic lattice motifs arising from a small set of conserved local interactions, triarylpyrylium salts can be considered both tunable and predictable solids for the design of anion-exchangeable materials. The electronic and conformational features of channel-forming triarylpyrylium cations revealed a competition between electrostatic and geometric stabilities, which results in a planar polyaryl building block with unique optical properties. Though the planarity of triarylpyrylium cations distinguishes these molecules from alternative arenes, the low resonance energy of the core heterocycle makes the pyrylium ring more susceptible to hydrolysis and rapid degradation, limiting the utility of solution-phase pyrylium-based anion receptors.

The conserved local motifs and unique extended structures formed by triarylpyrylium salts in the solid state were characterized and shown to display prerequisite features for solid-state anion exchange and capture, such as continuous cationic pore and channels with tunable electron density distributions about predicted C–H...X⁻ binding sites. These binding sites may be engineered through chemical substitution of the triarylpyrylium cation with retention of the local binding environment and functionally inconsequential modification of the extended structure. The specific effects of solvent-inclusion were addressed by careful analysis of the crystal structures of three solvated 2,4,6-tris(4-methylphenyl)pyrylium tetrafluoroborate salts. Additionally, co-crystallization of triarylpyrylium compounds with isosteric pyridine compounds was found to subtly modify common local motifs shared by triarylpyrylium salts to give rise to extended structures not observed in pure-phase triarylpyrylium salts. Co-crystallization also resulted in cationic pyrylium-based frameworks with reduced solubilities in aqueous media, making this material a candidate for heterogeneous anion exchange in the remediation of contaminated surface and groundwater systems. Modern anion exchange materials suffer from pH sensitivity and reduced performances in aqueous environments, which can be reduced in triarylpyrylium materials by co-crystallization. Though solid-state triarylpyrylium-based frameworks are a relatively unexplored area of anion exchange solids, they have already been shown to exhibit key properties that may side-step these engineering difficulties.

EXPERIMENTAL SECTION

All reagents were used as received from the manufacturer without further purification, with the exception of tetrahydrofuran and ethanol, which were dried over 3A molecular sieves. BHT-free biograde tetrahydrofuran, boron trifluoride diethyl etherate, and 48% (w/w) HBF_{4(aq)} were received from Alfa Aesar. Ethanol (200 proof, anhydrous), glacial acetic acid, and concentrated HCl were obtained from Pharmaco-Aaper. BHT-stabilized diethyl ether and toluene were purchased from Fischer Scientific. Ammonium acetate and 57% (w/w) HI_(aq) were purchased from Sigma-Aldrich, and 4-methylacetophenone and 4-methylbenzaldehyde were purchased from Eastman.

A Varian 400 MHz NMR spectrometer was used. All NMR spectra were taken at room temperature with spinning at 20 Hz. Shimming

and locking were performed using Varian VnmrJ software. A Rigaku Ultima IV diffractometer ($\lambda = 1.5418 \text{ \AA}$) with Bragg–Brentano geometry was used for room temperature PXRD experiments with a scan speed of $2^\circ/\text{min}$. Variable-temperature PXRD experiments were performed with parallel-beam geometry and kept under a flowing N_2 atmosphere. A scan-speed of $4^\circ/\text{min}$ was used for VT-PXRD experiments.

Single-Crystal X-ray Diffraction Methods. Data for compound **15a** were collected on a Bruker AXS D8 Quest CMOS diffractometer with a molybdenum $I\text{-}\mu\text{-S}$ microsource X-ray tube ($\lambda = 0.71073 \text{ \AA}$). Single crystal data for all other compounds (**15b–15d**) were collected using a Bruker AXS X8 Prospector CCD diffractometer with a copper $I\text{-}\mu\text{-S}$ microsource X-ray tube ($\lambda = 1.54178 \text{ \AA}$). Both feature laterally graded multilayer (Goebel) mirrors for monochromatization. Single crystals were mounted on Mitegen micromesh mounts with the help of a trace of mineral oil and flash cooled to 100 K.

The Apex2 software package was used to determine unit cells and for data collection, and data were integrated using SAINT. The data were processed with SADABS and corrected for absorption using multiscan techniques. The space groups were assigned using XPREP of the Bruker SHELXTL package, solved with ShelXD, and refined with SHELXL 2013 or 2014 and the graphical interface Shelxle. All non-hydrogen atoms were refined anisotropically. H atoms attached to carbon and hydroxyl oxygen atoms were positioned geometrically and constrained to ride on their parent atoms, with carbon hydrogen bond distances of 0.95 \AA for aromatic C–H, 0.99 and 0.98 \AA for aliphatic CH_2 and CH_3 , respectively. Methyl H atoms were allowed to rotate but not to tip to best fit the experimental electron density. $U_{\text{iso}}(\text{H})$ values were set to a multiple of $U_{\text{eq}}(\text{C/O})$ with 1.5 for CH_3 , and 1.2 for C–H.

All structures feature solvated anions within channels of the rigid frameworks. The residual electron density peaks corresponding to the solvent molecules occupying channels in the frameworks are highly disordered and often not arranged in an interpretable pattern. Complete crystallographic data, in CIF format, have been deposited with the Cambridge Crystallographic Data Centre. [CCDC 1444843–1444846](https://doi.org/10.1021/acs.cgd.6b00005) contain the supplementary crystallographic data for this paper. These data can be obtained free of charge from The Cambridge Crystallographic Data Centre via www.ccdc.cam.ac.uk/data_request/cif.

Synthesis of $\text{TMPPyry}^+ \text{BF}_4^-$. Adapted from the published literature.⁴³ 4-Methylacetophenone (91.8 mL, 92.26 g, 687.58 mmol) and 4-methylbenzaldehyde (40.3 mL, 41.07 g, 341.79 mmol) were refluxed in dry toluene (280 mL) and boron trifluoride diethyl etherate (86.96 mL) for 2 h during which time the golden starting solution rapidly converted to a deep red solution. A yellow solid precipitated upon addition of diethyl ether (yield: 59.1042 g, 134.86 mmol, 39.4%). $^1\text{H NMR}$ ($\text{D}_6\text{-Acetone}$, 400 MHz): δ (ppm) 2.538 (s, 6H), 2.538 (s, 3H), 7.623 (d, 2H), 7.642 (d, 4H), 8.471 (d, 4H), 8.523 (d, 4H), 9.066 (s, 2H).

Synthesis of TMPPy . Adapted from the published literature.⁴⁴ 4-Methylacetophenone (1.14 g, 8.50 mmol) and 4-methylbenzaldehyde (0.50 g, 4.16 mmol) were refluxed in 50 mL glacial acetic acid with excess ammonium acetate (7.27 g) for 16 h. Water was added to the cooled reaction solution, precipitating a cream-colored solid. Recrystallization from ethanol yielded white needles (yield: 0.2370 g, 0.678 mmol, 16.3%). $^1\text{H NMR}$ (CDCl_3 , 400 MHz): δ (ppm) 2.441 (s, 6H), 2.429 (s, 3H), 7.312 (d, 4H), 7.330 (d, 2H), 7.647 (d, 2H), 7.824 (s, 2H), 8.093 (d, 4H).

Crystallization of **15d.** Crystals were grown by dissolving 5 mg of $\text{TMPPyry}^+ \text{BF}_4^-$ and 5 mg TMPPy in 1 mL of a 1 THF: 1 diH_2O (v/v) mixed solvent by heating to 70°C . Once the compound was dissolved and the solvent mixture phase separated, the system was cooled to 4°C , crystallizing red rods with anisotropic hexagonal faces.

Crystallization of **15a.** Crystals were grown by dissolving 10 mg of $\text{TMPPyry}^+ \text{BF}_4^-$ in 1 mL of a 1 THF: 1 diH_2O (v/v) mixed solvent by heating to 70°C . Once the compound was dissolved and solvent phase separated, the mixture was cooled to 4°C , yielding gold rods with rhombic and orthorhombic faces.

Crystallization of **15b.** Crystals were grown by dissolving 15 mg of $\text{TMPPyry}^+ \text{BF}_4^-$ in 1 mL glacial acetic acid at 115°C . Once the $\text{TMPPyry}^+ \text{BF}_4^-$ was completely dissolved, the solution was cooled to 17°C , crystallizing gold rods.

Crystallization of **15c.** Crystals were grown by dissolving 3 mg $\text{TMPPyry}^+ \text{BF}_4^-$ in 1 mL ethanol with 5 drops of diH_2O at 80°C . Once the $\text{TMPPyry}^+ \text{BF}_4^-$ was completely dissolved, the solution was cooled to 17°C , yielding golden rods. Crystals grown from a dry ethanol solution had a blocky habit and exhibited non-Bragg behavior, preventing structural determination by single-crystal XRD. PXRD patterns of the needles and the block habits confirmed that the two habits are not isostructural.

■ ASSOCIATED CONTENT

Supporting Information

The Supporting Information is available free of charge on the ACS Publications website at DOI: [10.1021/acs.cgd.6b00005](https://doi.org/10.1021/acs.cgd.6b00005).

Details of the single-crystal structure determinations, structure factor tables, and Ortep-style plots for structures **15a–d** are included. Additionally, experimental and calculated PXRD diffractograms, a table of hydrogen-anion radial overlap values for **1–15c**, photographs of **15c** and **15d** crystallization, and further discussion of the anion exchange capabilities of **15d** (PDF)

Accession Codes

[CCDC 1444843–1444846](https://doi.org/10.1021/acs.cgd.6b00005) contains the supplementary crystallographic data for this paper. These data can be obtained free of charge via www.ccdc.cam.ac.uk/data_request/cif, or by emailing data_request@ccdc.cam.ac.uk, or by contacting The Cambridge Crystallographic Data Centre, 12 Union Road, Cambridge CB2 1EZ, UK; fax: +44 1223 336033.

■ AUTHOR INFORMATION

Corresponding Author

*Tel: (440) 775-8300. Fax: (440) 775-6682. E-mail: renwis@umich.edu.

Present Address

Department of Chemistry, University of Michigan, Ann Arbor, MI 48109, United States.

Notes

The authors declare no competing financial interest.

Dr. Jesse L. C. Rowsell passed away on January 30, 2015. Dr. Rowsell's curiosity toward questions that challenge present paradigms resulted in this research. His relentless dedication motivated the completion of this manuscript. The authors are grateful for his guidance in and outside of the lab.

■ ACKNOWLEDGMENTS

The X-ray diffractometers at Youngstown State University were funded by NSF Grants DMR-1337296, CHE-0087210, by Ohio Board of Regents Grant CAP-491, and by Youngstown State University. The powder X-ray diffractometer at Oberlin College was purchased with support of NSF grant DMR-0922588. Though the crystal structure for the co-crystal was solved from data collected at YSU, data were also collected at Beamline 15-ID B ChemMatCARS at the Advanced Photon Source through the Synchrotron Crystallography at the Advanced Photon Source, SCrAPS program supported by Indiana University. The authors would like to thank Drs. Maren Pink and Josh Chen for data collection and continued mentorship in addition to Drs. Adam J. Matzger and Antek G. Wong-Foy as well as Kyle A.

McDonald for their help during the completion of this manuscript.

REFERENCES

- (1) Oliver, S. R. *J. Chem. Soc. Rev.* **2009**, *38*, 1868–1881.
- (2) Fei, H.; Han, C. S.; Robins, J. C.; Oliver, S. R. *J. Chem. Mater.* **2013**, *25*, 647–652.
- (3) Moyer, B. A.; Custelcean, R.; Hay, B. P.; Sessler, J. L.; Bowman-James, K.; Day, V. W.; Kang, Sung-Ok. *Inorg. Chem.* **2013**, *52*, 3473–3490.
- (4) Zhao, X.; Bu, X.; Wu, T.; Zheng, S.; Wang, L.; Feng, P. *Nat. Commun.* **2013**, *4*, 1–9.
- (5) Custelcean, R.; Moyer, B. A. *Eur. J. Inorg. Chem.* **2007**, *10*, 1321–1340.
- (6) Custelcean, R. *Curr. Opin. Solid State Mater. Sci.* **2009**, *13*, 68–75.
- (7) Carlucci, L.; Ciani, G.; Maggini, S.; Proserpio, D. M.; Visconti, M. *Chem. - Eur. J.* **2010**, *16*, 12328–12341.
- (8) Fei, H.; Oliver, S. J. R. *Angew. Chem., Int. Ed.* **2011**, *50*, 9066–9070.
- (9) Li, X.; Xu, H.; Kong, F.; Wang, R. *Angew. Chem., Int. Ed.* **2013**, *52*, 13769–13773.
- (10) Lee, S.; Flood, A. H. *J. Phys. Org. Chem.* **2013**, *26*, 79–86.
- (11) Fairchild, R. M.; Holman, K. T. *J. Am. Chem. Soc.* **2005**, *127*, 16364–16365.
- (12) Li, Y.; Pink, M.; Karty, J. A.; Flood, A. H. *J. Am. Chem. Soc.* **2008**, *130*, 17293–17295.
- (13) Staffilani, M.; Bonvicini, G.; Steed, J. W.; Holman, K. T.; Atwood, J. L.; Elsegood, M. R. *J. Organometallics* **1998**, *17*, 1732–1740.
- (14) Atwood, J. L.; Holman, K. T.; Steed, J. W. *Chem. Commun.* **1996**, *12*, 1401–1407.
- (15) Li, Y.; Flood, A. *J. Am. Chem. Soc.* **2008**, *130*, 12111–12122.
- (16) Hirsch, B. E.; Lee, S.; Qiao, B.; Chen, C.; McDonald, K. P.; Tait, S. L.; Flood, A. H. *Chem. Commun.* **2014**, *50*, 9827–9830.
- (17) Holst, J. R.; Cooper, A. I. *Adv. Mater.* **2010**, *22*, 5212–5216.
- (18) McKeown, N. B. *J. Mater. Chem.* **2010**, *20*, 10588–10597.
- (19) Davis, M. E. *Nature* **2002**, *417*, 813–821.
- (20) Bradshaw, D.; Claridge, J. B.; Cussen, E. J.; Prior, T. J.; Rosseinsky, M. *Acc. Chem. Res.* **2005**, *38*, 273–282.
- (21) Lee, J.; Farha, O. K.; Roberts, J.; Scheidt, K. A.; Nguyen, S. T.; Hupp, J. T. *Chem. Soc. Rev.* **2009**, *38*, 1450–1459.
- (22) Murray, L. J.; Dincă, M.; Long, J. R. *Chem. Soc. Rev.* **2009**, *38*, 1294–1314.
- (23) Maji, T. K.; Matsuda, R.; Kitagawa, S. *Nat. Mater.* **2007**, *6*, 142–148.
- (24) Desiraju, G. R. *J. Am. Chem. Soc.* **2013**, *135*, 9952–9967.
- (25) Balaban, A. T.; Oniciu, D. C.; Katritzky, A. R. *Chem. Rev.* **2004**, *104*, 2777–2812.
- (26) Franconetti, A.; Contreras-Bernal, L.; Jatunov, S.; Gómez-Guillén, M.; Angulo, M.; Prado-Gotor, R.; Cabrera-Escribano, F. *Phys. Chem. Chem. Phys.* **2014**, *16*, 18442–18453.
- (27) El-Idreesy, T. T.; Clennan, E. L. *Photochem. Photobiol. Sci.* **2010**, *9*, 796–800.
- (28) Ionkin, A. S.; Marshall, W. J. *Organometallics* **2004**, *23*, 3276–3283.
- (29) Nunez Duran, C. N.; Rezende, M. C.; Vencato, I.; Neves, A. J. *Chem. Res., Synop.* **1998**, 698.
- (30) Beltran, A.; Isabel Burguete, M.; Abanades, D. R.; Perez-Sala, D.; Luis, S. V.; Galindo, F. *Chem. Commun.* **2014**, *50*, 3579–3581.
- (31) Müller, C.; Lopez, L. G.; Kooijman, H.; Spek, A. L.; Vogt. *Tetrahedron Lett.* **2006**, *47*, 2017–2020.
- (32) Ye, J.; Zhang, X.; Deng, D.; Ning, G.; Liu, T.; Zhuang, M.; Yang, L.; Gong, W.; Lin, Y. *RSC Adv.* **2013**, *3*, 8232.
- (33) Turowska-Tyrk, I.; Krygowski, T. M.; Milart, P.; Butt, G.; Topsom, R. D. *J. Mol. Struct.* **1991**, *245*, 289–299.
- (34) Krygowski, T. M.; Anulewicz, R.; Pniewska, B.; Milart, P. *J. Phys. Org. Chem.* **1991**, *4*, 121–124.
- (35) Ye, J.; Zhang, X.; Deng, D.; Ning, G.; Liu, T.; Zhuang, M.; Yang, L.; Gong, W.; Lin, Y. *RSC Adv.* **2013**, *3*, 8232–8235.
- (36) Kompan, O. E.; Potekhin, K. A.; Furmanova, N. G.; Struchkov, Y. T. *J. Struct. Chem.* **1980**, *21*, 195.
- (37) Turowska-Tyrk, I.; Anulewicz, R.; Krygowski, T. M.; Pniewska, B.; Milart, P. *Polym. J. Chem.* **1992**, *66*, 1831.
- (38) Malisza, K. L.; Top, S.; Vaissermann, J.; Caro, B.; Senéchal-Tocquer, M. C.; Senéchal, D.; Saillard, J. Y.; Kahlal, S.; Britten, J. F.; McGlinchey, M. J.; Jaouen, G. *Organometallics* **1995**, *14*, 5273–5280.
- (39) Tully, W.; Main, L.; Micholson, B. K. *J. Organomet. Chem.* **1996**, *507*, 103–115.
- (40) Frisch, M. J.; Trucks, G. W.; Schlegel, H. B.; Scuseria, G. E.; Robb, M. A.; Cheeseman, J. R.; Montgomery, J. A. Jr.; Vreven, T.; Kudin, K. N.; Burant, J. C.; Millam, J. M.; Iyengar, S. S.; Tomasi, J.; Barone, V.; Mennucci, B.; Cossi, M.; Scalamani, G.; Rega, N.; Petersson, G. A.; Nakatsuji, H.; Hada, M.; Ehara, M.; Toyota, K.; Fukuda, R.; Hasegawa, J.; Ishida, M.; Nakajima, T.; Honda, Y.; Kitao, O.; Nakai, H.; Klene, M.; Li, X.; Knox, J. E.; Hratchian, H. P.; Cross, J. B.; Bakken, V.; Amado, C.; Jaramillo, J.; Gomperts, R.; Stratmann, R. E.; Yazyev, O.; Austin, A. J.; Cammi, R.; Pomelli, C.; Ochterski, J. W.; Ayala, P. Y.; Morokuma, K.; Voth, G. A.; Salvador, P.; Dannenberg, J. J.; Zakrzewski, V. G.; Dapprich, S.; Daniels, A. D.; Strain, M. C.; Farkas, O.; Malick, D. K.; Rabuck, A. D.; Raghavachari, K.; Foresman, J. B.; Ortiz, J. V.; Cui, Q.; Baboul, A. G.; Clifford, S.; Cioslowski, J.; Stefanov, B. B.; Liu, G.; Liashenko, A.; Piskorz, P.; Komaromi, I.; Martin, R. L.; Fox, D. J.; Keith, T.; Al-Laham, M. A.; Peng, C. Y.; Nanayakkara, A.; Challacombe, M.; Gill, P. M. W.; Johnson, B.; Chen, W.; Wong, M. W.; Gonzalez, C.; Pople, J. A. *GAUSSIAN03*; Gaussian Inc.: Wallingford, CT, USA, 2004.
- (41) Desiraju, G. R. *Acc. Chem. Res.* **1996**, *29*, 441–449.
- (42) Rowland, R. S.; Taylor, R. *J. Phys. Chem.* **1996**, *100*, 7384–7391.
- (43) Bello, A. M.; Kotra, L. P. Improved synthesis of pyrylium salts leading to 2,4-disubstituted diaryl via novel mechanism. *Tetrahedron Lett.* **2003**, *44*, 9271–9274.
- (44) Yang, C.; Lee, I.; Chen, T.; Chien, W.; Hong, J. J. *J. Mater. Chem. C* **2013**, *1*, 2842–2850.
- (45) Katritzky, A. R. Short Course in Heterocyclic Chemistry, Lecture 10 Lecture Slides. 1–54 (<http://ocw.mit.edu/courses/chemistry/5-12-organic-chemistry-i-spring-2003/lecture-handouts/>).
- (46) Balaban, A. T. Unpublished. 2011, 402–419.